Letters

A General Analytical Model of Single-Layer Common-Mode Chokes

Qiao Li, *Member, IEEE*, Biyan Xie, *Student Member, IEEE*, Yechi Zhang, *Member, IEEE*, Jun Ma, *Member, IEEE*, and Chao Yuan, *Member, IEEE*

***Abstract*—To accurately model common-mode (CM) chokes is crucial for ensuring the design and optimization of EMI filters. This letter identifies the limitations of the commonly employed analytical model, which results in significant margin errors when applied to CM chokes. It proposes a comprehensive and more precise analytical model that addresses these errors by considering the influence of time-varying electromagnetic fields and the geometric characteristics of CM chokes. Furthermore, this letter provides a detailed explanation of the physical significance behind the proposed model. Both methods are compared, and the suggested approach is validated through simulations and experiments in four distinct scenarios.**

***Index Terms*—Circuit model, common-mode (CM) chokes, electromagnetic analysis, electromagnetic interference (EMI).**

I. Introduction

NOWADAYS,trends in designing power electronic devices for lightweight and compact size have led to higher switching frequencies, necessitating stricter compliance with electromagnetic interference (EMI) standards [1]. Operating at high frequencies (HF), common-mode (CM) chokes exhibit substantial deviations from the ideal model due to parasitic capacitance related to windings and magnetic cores, leakage inductances, relative permittivity, and permeability of the core. These factors significantly elevate the EMI levels [2], [3]. Therefore, accurately modeling CM chokes is essential to optimize EMI filters effectively and enable devices to meet EMI standards without increasing their weight and size.

Existing models for HF CM chokes can be broadly categorized into two main types: behavioral and physical models [4], [5]. Among physical modeling methods, the finite element method (FEM) offers high accuracy but demands substantial computational resources [6], [7]. Consequently, analytical methods are more promising. The most renowned and highly cited analytical model for CM chokes was developed by Kovacic et al. [8]. This model incorporates parameters related to individual winding turns, considers magnetic core material properties, and accounts for mutual coupling among turns and the core. It offers significant design advantages by directly calculating parameters based on geometry. However, the accuracy of the impedance curve decreases when dealing with CM chokes having a small number of turns and different materials, which raises concerns due to the increasing significance of such chokes in power electronic devices with higher switching frequencies and lower inductance requirements [1].

In HF operation, parasitic capacitance plays a pivotal role in the characteristics of CM chokes [9], [10]. Consequently, numerous studies have been conducted to calculate and model parasitic capacitance [11], [12]. In a study [3], the calculated capacitance consistently fell short of the measured capacitance when the number of turns was small. The discrepancy, attributed to time-varying electromagnetic fields inside the core, was extensively discussed in [14]. In summary, accounting for the effects of time-varying electromagnetic fields is crucial when modeling CM chokes. In particular, among CM inductors, MnZn cores are dominated by core capacitance while nanocrystals are dominated by space capacitance.

The rest of this letter is organized as follows. In Section II, the analytical model of CM chokes is introduced in detail. Based on the analysis presented above, in Section III, verification and discussion are conducted among the traditional model, the proposed general model, FEM results, and experimental data. Finally, Section IV concludes this letter.

II. Analytical Modeling

A. Electromagnetic Behavior of CM Chokes and Derivation of HF Circuit Model

Fig. 1 illustrates the key geometric parameters of a toroidal CM choke. In this letter, considering the actual geometric structure, the real magnetic core chamfers have been taken into consideration. In the subsequent sections, an enhanced equivalent circuit for modeling CM chokes will be presented, the physical significance of parameters in the proposed circuit model will be discussed, and the calculations for inductance, space capacitance correction, and core capacitance will be explored.

Manuscript received 11 January 2024; revised 11 February 2024; accepted 27 February 2024. Date of publication 1 March 2024; date of current version 19 April 2024. This work was supported by the National Natural Science Foundation of China under Grant 52107189. *(Corresponding author: Yechi Zhang.)*

Qiao Li, Biyan Xie, and Chao Yuan are with the College of Electrical and Information Engineering, Hunan University, Changsha 410082, China (e-mail: qiaoli@hnu.edu.cn).

Yechi Zhang is with Dalian Maritime University, Dalian 116026, China (e-mail: zhangyc@dlmu.edu.cn).

Jun Ma is with the Department of Electrical and Electronic Engineering, University of Bristol, BS8 1QU Bristol, U.K.

Color versions of one or more figures in this article are available at https://doi.org/10.1109/TPEL.2024.3372297.

Digital Object Identifier 10.1109/TPEL.2024.3372297

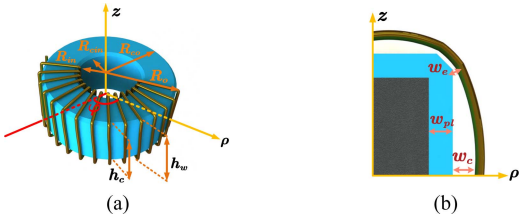

Fig. 1. Geometry and cross section of a toroidal CM choke. (a) Geometry of CM choke. (b) Cross section of CM choke. R_o and R_{co} are the outer radius of CM choke. R_{in} and R_{cin} is inner radius of CM choke. w_c is maximum distance between turn and core. w_e is minimum distance between turn and core.

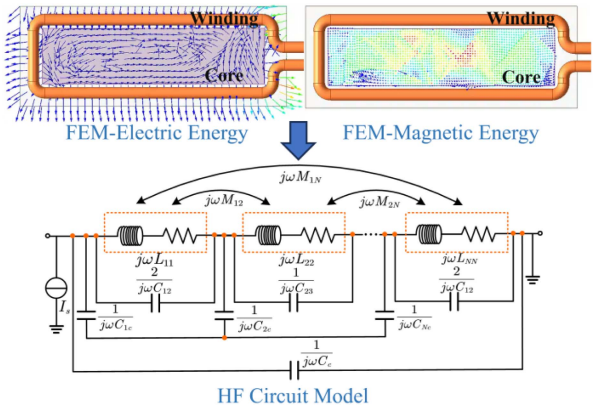

Fig. 2. Proposed equivalent circuit model.

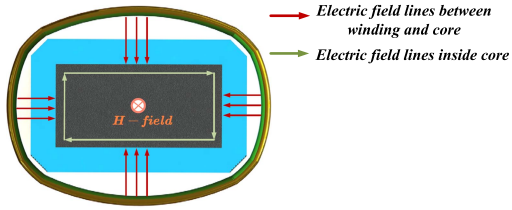

Fig. 3. Distribution of electric field lines in cross section of a toroidal CM choke.

For a CM choke, the primary concern lies in its inductive performance, as illustrated in Fig. 2, representing the magnetic field energy within it. However, in high-frequency (HF) scenarios, the presence of displacement currents leads to the existence of electric field energy between turns and between turns and the core. This corresponds to the turn-to-turn capacitance (C_{tt}) and the turn-to-core capacitance (C_{tc}), respectively. Furthermore, due to the time-varying electromagnetic field, a time-varying electric field emerges inside the core, which equivalently corresponds to the core capacitance (C_c). Several studies have addressed the presence of C_c [3], [14]. However, in [8], analytical modeling techniques for CM chokes neglect the existence of C_c, rendering them suitable only for a large number of turns. When dealing with fewer turns, the accuracy of the modeling significantly diminishes. In addition, all capacitance derivations are based on simplified geometry, resulting in reduced accuracy. In [14], C_c has been discussed, and its relationship with the number of turns has been explored, but no consideration has been given to how C_c should be incorporated into the circuit model and its relationship with different materials. Therefore, a more comprehensive circuit model is developed here, and a detailed discussion on whether C_c should be disregarded for different materials is presented in Section III. Furthermore, the physical implications of constructing circuit models will be thoroughly explored.

The general circuit model is depicted in Fig. 2. In this model, each turn is treated as an independent unit, comprising self-inductance (L_s) and core losses (R_s) in series, along with C_{tt} in parallel. One end of C_{tc} is connected to the left-hand side of the unit, while the other end shares a common node with other C_{tc}. Since the last turn lacks an adjacent turn, the turn-to-turn capacitance between the first and second turns is divided into two equal parts. One part is in parallel with the last turn, with each part representing half of the turn-to-turn capacitance. When considering the general inductor in which the core is completely wound, the last turn does not lack the adjacent turn any more due to the distance between the last turn and the first turn got smaller. The capacitance that originally needed to be changed to half does not need to be halved again. The turn-to-turn capacitance of the last turn becomes the capacitance between the last turn and the first turn $C_{N,1}$. As illustrated in Fig. 2, FEM is applied to reveal the distribution of electric field lines within a CM choke cross section. It is obvious that the electric field lines distributed in space between winding and core is perpendicular to and terminate at the surface of core, which is an equipotential surface, while rectangle closed electric field line distributes inside the core. However, these two sources of electric field lines are not the same. In space between winding and core, electric field lines terminate and perpendicular to the surface of the conductor, and the entire surface of the core can be treated as equipotential, as illustrated in Fig. 3. That is because perfect conductor assumption is commonly applied to CM chokes due to their high permeability and permittivity. As per this assumption, under the influence of a static electric field, charge is distributed over the surface of the conductor, resulting in a net electric field inside the conductor being zero. Meanwhile, inside the core, Faraday's law dictates that electric field lines are always perpendicular to the magnetic field, thereby forming a continuous closed curve to ensure tangential continuity at the boundary. The electric field lines run parallel to the boundary of the core cross section, creating a rectangular closed curve. The two electric field lines do not intersect or interfere. Thus, that is the reason why C_c generated by the time-varying electric field can only be connected in parallel to the first and last turns of the winding from an energy perspective and C_{tc} have a common node, reflecting the equipotential surface. As a result, the impedance curve can be determined using circuit analysis methods at each frequency.

Upon the completion of the circuit model construction, the subsequent parameter extraction process is carried out. In traditional models, capacitance is often extracted using simplified geometries, resulting in significant errors in both capacitance and impedance curves, as will be demonstrated in Section III.

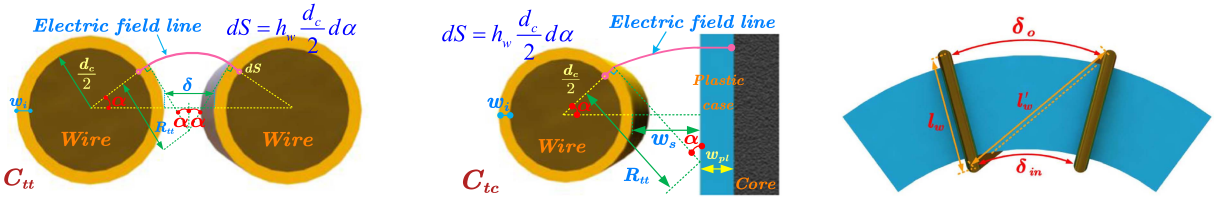

Fig. 4. Geometry between turns, turns and core of a toroidal CM choke. (a) Geometry between turns. (b) Geometry between turns and core. (c) Geometry in the lateral region of CM choke. d_c represents the radius of the conductor, w_i stands for the thickness of wire insulation. w_{pl} represents the thickness of core insulation. ϵ_{pl} denotes the relative permittivity of the core insulation. ϵ_a denotes the relative permittivity of air. ϵ_i signifies the relative permittivity of the wire insulation. l_w is winding length parallel to choke.

Therefore, the consideration of the actual geometry, which includes complete insulation, winding bends, and helix lengths, is undertaken to improve the model's accuracy.

B. Complex Inductance Modeling

The complex relative permeability of the core is a crucial factor in inductance modeling, represented by its real part μ_r', and its imaginary part μ_r". Consequently, the impedance (Z) of a single turn, when neglecting winding losses, can be expressed as follows:

$$Z = j\omega L_s + R_s \tag{1}$$

According to Ampère's circuital law, Z can be further expressed as follows:

$$Z = \mu_0(\mu_r' - j\omega\mu_r'')\frac{h_c}{2\pi}\ln\left(\frac{R_o}{R_{\text{in}}}\right). \tag{2}$$

Within CM chokes, the self-inductance of a single turn can be denoted as L_{ii}, while the leakage inductance between turn i and turn j is represented as $L_{\sigma ij}$, and the mutual inductance between turn i and turn j is expressed as M_{ij}. The relationships among these parameters are as follows:

$$L_{ii} = M_{ij} + L_{\sigma ij}. \tag{3}$$

In this letter, the neglect of leakage inductance is justified due to its orders of magnitude smaller magnitude compared with self-inductance.

C. Space Capacitance Modeling

In an effort to mitigate the detrimental impact of parasitic capacitance at HF, numerous studies have endeavored to precisely uncover its underlying mechanisms and develop models. Nonetheless, existing analytical models often encounter issues related to their applicability and lack of comprehensive consideration for various factors. For instance, questions arise regarding whether the model can be applied to single-layer chokes or if it accounts for actual electric field lines, the true geometry between turns, and the core, insulations, and winding transitions. To achieve a more accurate model, contributions have been made by taking into account winding insulation, the actual turn-to-core distance, and the actual winding length.

As depicted in Fig. 4, C_{tt} and C_{tc} in different material regions can be analytically calculated using the following methods:

$$dC = \varepsilon_0 dS / \sum_i (x_i/\varepsilon_{ri}) \tag{4}$$

where dS represents the differential area, x denotes the electric lines path, and ϵ_r is the relative permittivity of the medium. Building upon the theory presented in [8], in the calculation of parasitic capacitance, three distinct regions can be identified, which are outer region (C_{tto}, C_{tco}), inner region (C_{ttin}, C_{tcin}), and lateral region (C_{ttl}, C_{tcl}). However, it does not consider winding insulation. As shown in Fig. 2, the geometry between turns, and turns and the core is clearly illustrated. When accounting for winding insulation, C_{tt} can be re-expressed as follows:

$$C_{tt} = C_{tto} + C_{ttin} + C_{ttlw} + C_{ttl'w} \tag{5}$$

where C_{ttlw} is the fixed segment turn-to-turn capacitance parallel to one side of the core, and $C_{ttl'w}$ is the corrected segment turn-to-turn capacitance parallel to another side of the core. In accordance with (4), the first step in the determination of the capacitance is the determination of the length of the electric field lines in the corresponding medium. As shown in Fig. 4(a), the radius of the arc of the electric line R_{tt} in the air can be expressed as a function of φ

$$R_{tt} = \left[\frac{\delta}{2} + \left(\frac{d_c}{2} + w_i\right)(1-\cos\alpha)\right]\frac{1}{\sin\alpha}. \tag{6}$$

Then, the length of the arc of the electric line x_{tt} can be expressed as

$$x_{tt} = 2\alpha R_{tt} = \frac{\alpha[\delta + (d_c + 2w_i)(1-\cos\alpha)]}{\sin\alpha}. \tag{7}$$

Hence, the inner turn-to-turn capacitance C_{ttin} and outer turn-to-turn capacitance C_{tto} can be expressed, respectively, as

$$\begin{cases} C_{tto} = \int_{-\frac{\pi}{2}}^{\frac{\pi}{2}} \frac{\varepsilon_0\varepsilon_i\varepsilon_a h_w (d_c/2)\sin\alpha d\alpha}{2w_i\varepsilon_a\sin\alpha + \alpha\varepsilon_i[\delta_o + (d_c+2w_i)(1-\cos\alpha)]} \\ C_{ttin} = \int_{-\frac{\pi}{2}}^{\frac{\pi}{2}} \frac{\varepsilon_0\varepsilon_i\varepsilon_a h_w (d_c/2)\sin\alpha d\alpha}{2w_i\varepsilon_a\sin\alpha + \alpha\varepsilon_i[\delta_{\text{in}} + (d_c+2w_i)(1-\cos\alpha)]}. \end{cases} \tag{8}$$

For a winding first fixed on one side parallel to the core, the equation for the electric field lines between turns can be

expressed as follows:

$$\delta(r) = \frac{\delta_o - \delta_{\text{in}}}{R_o - R_{\text{in}}}(r - R_{\text{in}}) + \delta_{\text{in}}. \tag{9}$$

Then, C_{ttlw} can be expressed as follows:

$$C_{ttlw} = \int_{R_{\text{in}}}^{R_o} \int_{-\frac{\pi}{2}}^{\frac{\pi}{2}} \frac{\varepsilon_0 \varepsilon_i \varepsilon_a (d_c/2) \sin\alpha d\alpha}{\alpha\varepsilon_i[\frac{\delta_o - \delta_{\text{in}}}{R_o - R_{\text{in}}}(r - R_{\text{in}}) + \delta_{\text{in}} + (d_c + 2w_i)(1 - \cos\alpha)] + 2w_i\varepsilon_a}. \tag{10}$$

The length of the winding on the other side corrected is l'_w. Due to the complexity of the calculation thought the error is small, we can approximate the angle of two adjacent turns equal to φ and the intersection point is assumed to be at the center of the core. Thus, the equation for the electric field lines between turns can be expressed as follows:

$$\delta'(r) = \frac{\delta_o - \delta_{\text{in}}}{l'_w}(r - R_{\text{in}}) + \delta_{\text{in}}. \tag{11}$$

The capacitance $C_{ttl'w}$ can be expressed as

$$C_{ttl'w} = \int_{R_{\text{in}}}^{R_{\text{in}} + l'_w} \int_{-\frac{\pi}{2}}^{\frac{\pi}{2}} \frac{\varepsilon_0 \varepsilon_i \varepsilon_a (d_c/2) \sin\alpha d\alpha}{\alpha\varepsilon_i[\frac{\delta_o - \delta_{\text{in}}}{l'_w}(r - R_{\text{in}}) + \delta_{\text{in}} + (d_c + 2w_i)(1 - \cos\alpha)] + 2w_i\varepsilon_a}. \tag{12}$$

C_{tc} is essentially the same as the C_{tt}, and C_{tc} can be re-expressed as follows:

$$C_{tc} = C_{tco} + C_{tcin} + C_{tclw} + C_{tcl'w}. \tag{13}$$

The radius of the arc of the electric line R_{tc} in the air can be expressed as a function of α

$$R_{tc} = [w_s + \left(\frac{d_c}{2} + w_i\right)(1 - \cos\alpha)]\frac{1}{\sin\alpha}. \tag{14}$$

Then, the length of the arc of the electric line x_{tc} can be expressed as

$$x_{tc} = \alpha R_{tc} = \frac{\alpha[w_s + (\frac{d_c}{2} + w_i)(1 - \cos\alpha)]}{\sin\alpha}. \tag{15}$$

Hence, the inner turn-to-core capacitance C_{tcin} and outer turn-to-core capacitance C_{tco} can be expressed, respectively, as

$$\begin{cases} C_{tco} = \int_{-\frac{\pi}{2}}^{\frac{\pi}{2}} \frac{\varepsilon_0 h_w (d_c/2)\varepsilon_a\varepsilon_i\varepsilon_{pl}\sin\alpha d\alpha}{\alpha\varepsilon_i\varepsilon_{pl}[w_{so} + (d_c/2 + w_i)(1 - \cos\alpha)] + \varepsilon_a \sin\alpha(\varepsilon_{pl}w_i + \varepsilon_i w_{pl})} \\ C_{tcin} = \int_{-\frac{\pi}{2}}^{\frac{\pi}{2}} \frac{\varepsilon_0 h_w (d_c/2)\varepsilon_a\varepsilon_i\varepsilon_{pl}\sin\alpha d\alpha}{\alpha\varepsilon_i\varepsilon_{pl}[w_{\sin} + (d_c/2 + w_i)(1 - \cos\alpha)] + \varepsilon_a \sin\alpha(\varepsilon_{pl}w_i + \varepsilon_i w_{pl})}. \end{cases} \tag{16}$$

Same process as the derivation of C_{tt}, then C_{tclw} can be expressed as

$$C_{tclw} = \int_{-\frac{\pi}{2}}^{\frac{\pi}{2}} \frac{\varepsilon_0 (R_o - R_{in})(d_c/2)\varepsilon_a\varepsilon_i\varepsilon_{pl}\sin\alpha d\alpha}{\alpha\varepsilon_i\varepsilon_{pl}[w_{sl} + (d_c/2 + w_i)(1 - \cos\alpha)] + \varepsilon_a \sin\alpha(\varepsilon_{pl}w_i + \varepsilon_i w_{pl})}. \tag{17}$$

The capacitance $C_{tcl'w}$ can be expressed as

$$C_{tcl'w} = \int_{-\frac{\pi}{2}}^{\frac{\pi}{2}} \frac{\varepsilon_0 l'_w (d_c/2)\varepsilon_a\varepsilon_i\varepsilon_{pl}\sin\alpha d\alpha}{\alpha\varepsilon_i\varepsilon_{pl}[w_{sl} + (d_c/2 + w_i)(1 - \cos\alpha)] + \varepsilon_a \sin\alpha(\varepsilon_{pl}w_i + \varepsilon_i w_{pl})}. \tag{18}$$

As depicted in Fig. 1(b), because the conductor is not evenly fitted to the core, there is a need to adjust the distance between turns and the core. However, in traditional models, winding transitions are often overlooked. Therefore, in this letter, capacitive equivalence is employed, allowing for the derivation of an equivalent turn-to-core distance [13]

$$w'_s = 2\sqrt{w_c(w_c - w_e)} / \log\left(\frac{\sqrt{w_c} + \sqrt{w_c - w_e}}{\sqrt{w_c} - \sqrt{w_c - w_e}}\right). \tag{19}$$

Furthermore, in the traditional model, the coil length is typically assumed to be the perimeter of a rectangle. However, during the winding process, the coil length in the parallel region does not directly correspond to half of the difference between the inner and outer diameters of the inductor. Therefore, this letter incorporates corrections, as shown in Fig. 4(c). The length of l'_w can be calculated using the cosine theorem

$$l'^2_w = 2R^2_{\text{in}}(1 - \cos\varphi) + (R_o - R_{\text{in}})^2 - 2\sqrt{2(1 - \cos\varphi)}R_{\text{in}}(R_o - R_{\text{in}})\cos((\pi + \varphi)/2). \tag{20}$$

The calculation of C_{tt} and C_{tc} using the proposed general model, the traditional model presented in [8], and FEM simulations (*Ansys Maxwell*) is illustrated in Fig. 5. The parameters of FEM model are presented in Table I. The errors in dC_{tt}, dC_{tc}, C_{tt}, and C_{tc} obtained by the traditional model are 28.6%, 8.8%, 16.2%, and 26.2%, respectively. In contrast, the errors in the proposed general model are 8.3%, 0.1%, 2.4%, and 0.5%, respectively. These results unequivocally demonstrate the significantly higher accuracy achieved by the proposed model.

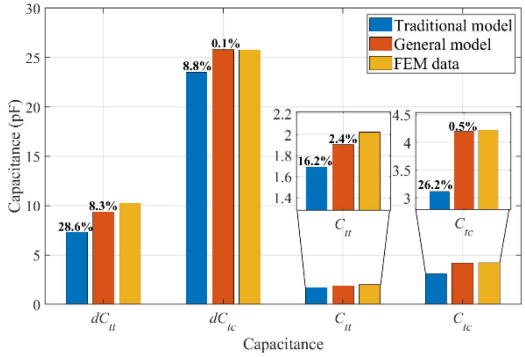

Fig. 5. Comparison among traditional model, proposed general model, and FEM obtained space capacitance.

TABLE I
PARAMETERS OF FEM MODEL

Core permittivity	12000
Dimension	50/40/20 (mm)
Number of turns	16
Core insulation	1.5 mm
Winding insulation	0.1 mm
Equivalent turn-to-core distance	0.2 mm
Diameter of winding	1 mm
Angle between turns	~6°

D. Core Capacitance Modeling

In accordance with the principles described in [12], an equivalent capacitance can be determined based on the energy associated with the time-varying electric field

$$C_c = \varepsilon_0 \varepsilon_r l/8/\pi/N^2. \tag{21}$$

In this formula, ϵ_r represents the relative permittivity of the core, l is the equivalent circumference of the core, and N is the number of turns. This equation clarifies that C_c depends not only on the number of turns but also on the permittivity of core materials. In addition, it is evident that the core capacitance is not influenced by the shape of the core's cross section, making it applicable to CM chokes. However, it is important to note that the first resonant frequency, at which C_c becomes the dominant factor in the equivalent parasitic capacitance, may need adjustment due to the inductance associated with the cross-sectional shape of the core. In most applications, common mode cores are rectangular in cross section. Therefore, it is necessary to correct this equation for rectangular cross sections. A formula for the first resonance point, denoted as f_R and tailored for rectangular cross sections, is derived, which is suitable for widely used CM chokes

$$f_R = \sqrt{1/(L \cdot C_M)}/(2\pi). \tag{22}$$

Then, the formula for calculating the inductance of a rectangular cross-sectional core is usually given by

$$L = \mu \cdot h \cdot N^2 \cdot \ln\left(\frac{R_o}{R_{\text{in}}}\right)/2/\pi. \tag{23}$$

Substituting (23) and (21) into (22) yields

$$f_R = 2/\sqrt{\mu_0 \mu_r \varepsilon_0 \varepsilon_r l h \ln(R_o/R_{\text{in}})}. \tag{24}$$

III. VERIFICATION AND DISCUSSION

Toroidal CM chokes with different numbers of turns, ranging from fewer turns to more turns tightly wound, have been manufactured, as depicted in the Fig. 6 and detailed in Table II, which is also the parameters of FEM model simulated by *Ansys HFSS*. The testing equipment employed for these chokes is the WAYNE KERR 6500B impedance analyzer, covering a frequency range between 150 kHz and 30 MHz.

The testing results, as depicted in Fig. 7, clearly indicate that when examining CM chokes with 15 turns, the impedance curves generated by the proposed general model and the conventional model exhibit minimal discrepancies when compared

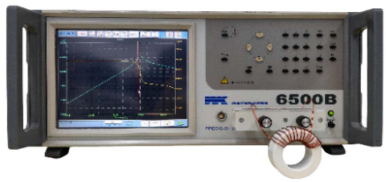

Fig. 6. Equipment and core used for experiments.

TABLE II
PARAMETERS OF TOROIDAL CM CHOKES [15], [16], [17]

	MnZn 3C94		Nanocrystal W516	Nanocrystal CC108
Core permittivity	2×10^5~5×10^4		~10	
Core permeability	1.5×10^3~2×10		2×10^4~2×10^2	2×10^3~3×10^2
Dimension	50/30/19 (mm)		50/40/20 (mm)	45/22/18 (mm)
Number of turns	15	4	34	6
Core insulation	0.5 mm			
Winding insulation	0.1 mm			
Equivalent turn-to-core distance	0.2 mm			
Diameter of winding	1 mm			

with experimental data. However, the situation differs for chokes with four turns. In the case of four-turn chokes, there is a 600 kHz difference in the resonance point frequencies between the impedance curves derived from the two methods. The proposed general model displays a 4% error when compared with the measured data, whereas the traditional model yields an error of 33%. When dealing with chokes containing 15 turns, the resonance frequencies between the impedance curves generated by the two methods differ by 50 kHz. The proposed general model displays a 3% error compared with the measured data, whereas the traditional model results in an error of 4.6%. In contrast, the general model consistently demonstrates significantly higher accuracy, particularly for CM chokes with a lower number of turns.

As depicted in Fig. 8, in order to assess the general applicability of the proposed model, tests were conducted on two cores made from nanocrystalline materials. It is apparent that both the traditional model still exhibits significant errors when compared with the measured data and the general model, regardless of the number of turns considered. When dealing with chokes containing six turns, the error of our proposed general model in comparison to the measured data is 2.3%, whereas the traditional model yields an error of 45.1%. For chokes with 34 turns, the error of our proposed general model is 0.8%, while the traditional model results in an error of 25.3%. In these instances, significantly higher accuracy is consistently demonstrated by the proposed general model. Comparing these results with MnZn, it can be attributed to the fact that nanocrystalline materials possess low permittivity, resulting in minimal impedance impact. However, in this scenario, space capacitance plays a dominant role, leading to a significant error in the impedance curve, as illustrated in Fig. 8. It is feasible to recalibrate the space capacitance formula by considering the actual geometry.

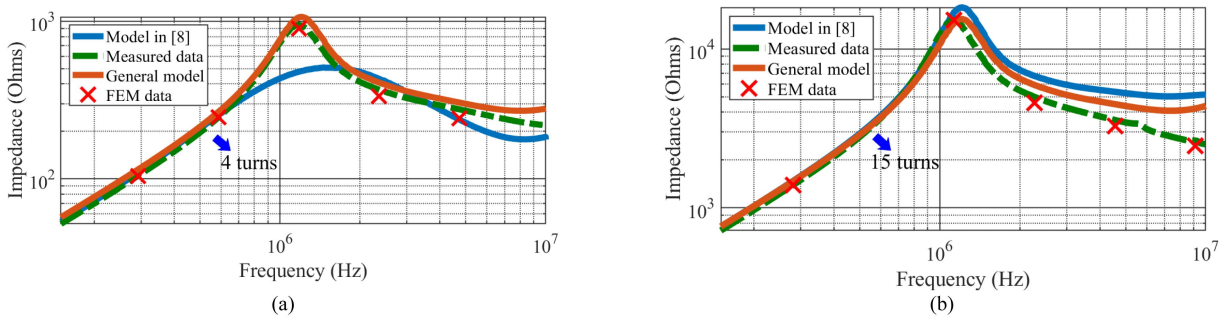

Fig. 7. Comparison among measured, traditional model, general model, and FEM obtained impedance (MnZn). (a) Four turns. (b) Fifteen turns.

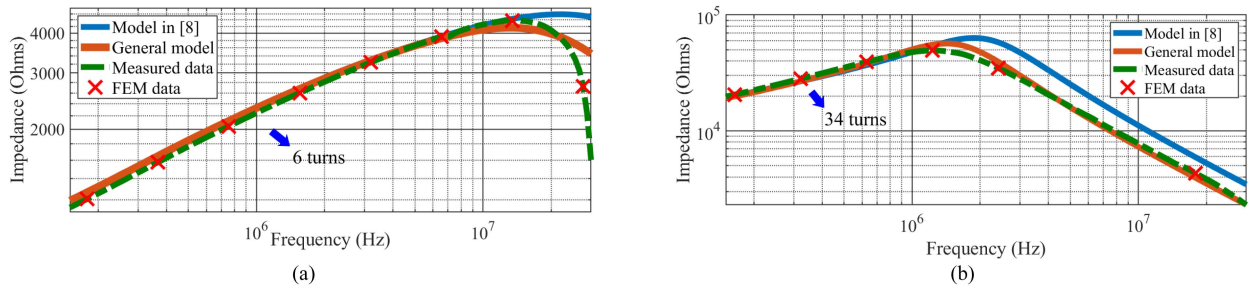

Fig. 8. Comparison among measured, traditional model, general model, and FEM obtained impedance (Nanocrystal). (a) Six turns. (b) Thirty-four turns.

IV. Conclusion

This letter presents a comprehensive analytical model for single-layer CM chokes, aiming to overcome the limitations of traditional models and providing a detailed discussion of the model's physical significance. The proposed model addresses the influence of time-varying electromagnetic fields and integrates advanced techniques for deriving internal lumped parameters. To enhance accuracy, the model takes into account the actual geometric characteristics. Through simulation and experimental results involving various materials, the high modeling accuracy of the proposed general model for CM chokes with different geometries, core materials, and varying numbers of turns is convincingly demonstrated.

References

[1] Y. Zhang, Q. Li, and D. Jiang, "A motor CM impedance based transformerless active EMI filter for DC-side common-mode EMI suppression in motor drive system," *IEEE Trans. Power Electron.*, vol. 35, no. 10, pp. 10238–10248, Oct. 2020.

[2] Z. Shen et al., "Core energy capacitance of NiZn inductors," *IEEE Trans. Power Electron.*, vol. 38, no. 4, pp. 4235–4240, Apr. 2023.

[3] Y. Li and S. Wang, "Modeling and increasing the high-frequency impedance of single-layer Mn-Zn ferrite toroidal inductors with electromagnetic analysis," *IEEE Trans. Power Electron.*, vol. 36, no. 6, pp. 6943–6953, Jun. 2021.

[4] Á. Ojeda-Rodríguez, J. Bernal-Méndez, and M. A. Martín-Prats, "Modal theory and approach for accurate characterization of common-mode chokes," *IEEE Trans. Power Electron.*, vol. 38, no. 9, pp. 10516–10529, Sep. 2023.

[5] X. Liu et al., "Behavioral modeling of complex magnetic permeability with high-order Debye model and equivalent circuits," *IEEE Trans. Electromagn. Compat.*, vol. 63, no. 3, pp. 730–738, Jun. 2021.

[6] N. Moonen, R. Vogt-Ardatjew, A. Roc'h, and F. Leferink, "3-D full-wave high frequency common mode choke modeling," *IEEE Trans. Electromagn. Compat.*, vol. 62, no. 3, pp. 707–714, Jun. 2020.

[7] H. Jie et al., "Characterization and modeling of single-phase common-mode chokes via finite-element analysis," in *Proc. 49th Annu. Conf. IEEE Ind. Electron. Soc.*, 2023, pp. 1–6.

[8] M. Kovacic, Z. Hanic, S. Stipetic, S. Krishnamurthy, and D. Zarko, "Analytical wideband model of a common-mode choke," *IEEE Trans. Power Electron.*, vol. 27, no. 7, pp. 3173–3185, Jul. 2012.

[9] H. Jie et al., "High-precision broadband impedance measurements of three-phase common-mode chokes using single-port circuit de-embedding and three-port network calibration methods," *IEEE Trans. Ind. Electron.*, early access, Oct. 23, 2023, doi: 10.1109/TIE.2023.3322008.

[10] H. Jie et al., "VNA-based fixture adapters for wideband accurate impedance extraction of single-phase EMI filtering chokes," *IEEE Trans. Ind. Electron.*, vol. 70, no. 8, pp. 7821–7831, Aug. 2023.

[11] S. Luan, Z. Yan, and H. Zhao, "Effects of airgaps on parasitic capacitance of magnetic components," *IEEE Trans. Power Electron.*, vol. 39, no. 1, pp. 1115–1134, Jan. 2024.

[12] H. Zhao et al., "Physics-based modeling of parasitic capacitance in medium-voltage filter inductors," *IEEE Trans. Power Electron.*, vol. 36, no. 1, pp. 829–843, Jan. 2021.

[13] F. Salomez, A. Videt, and N. Idir, "Modeling and minimization of the parasitic capacitances of single-layer toroidal inductors," *IEEE Trans. Power Electron.*, vol. 37, no. 10, pp. 12426–12436, Oct. 2022.

[14] R. Zhang, S. Wang, T. Long, J. Qiu, K. Liu, and H. Zhao, "The magnetized capacitance, first resonant frequency, and electromagnetic analysis of inductors with ferrite cores," *IEEE Trans. Ind. Electron.*, vol. 71, no. 6, pp. 5734–5744, Jun. 2024.

[15] Ferroxcube, "Data handbook," 2017. [Online]. Available: https://www.ferroxcube.com/zh-CN/download/download/21

[16] Vacuumschmelze, "Soft magnetic materials and semi-finished products," 2021. [Online]. Available: https://vacuumschmelze.com/03_Documents/Brochures/PHT%20001%20en.pdf

[17] Vacuumschmelze, "EMC products based on nanocrystalline VITROPERM," 2021. [Online]. Available: https://vacuumschmelze.com/03_Documents/Brochures/EMC%20Products%20based%20on%20Nanocrystalline%20VITROPERM.pdf